Electronic Supplementary Material (ESI) for Nanoscale.

Supporting Information

Ni/TiO$_2$ Heterostructure Derived from Phase Separation for Enhanced Electrocatalysis of Hydrogen Evolution and Biomass Oxidative Upgrading in Anion Exchange Membrane Electrolyzer

Geng Zhang,[a,#] Rui Yu,[a,#] Yu-Qi Zhou,[a,#] Wang-Ting Lu,[b,c], Fei-Fei Cao[a,*]

[a] College of Chemistry, Huazhong Agricultural University, 430070, Wuhan, P. R. China.

[b] Key Laboratory of Optoelectronic Chemical Materials and Devices, Ministry of Education, Jianghan University, 430056, Wuhan, P. R. China.

[c] Institute for Interdisciplinary Research, School of Optoelectronic Materials and Technology, Jianghan University, 430056, Wuhan, P. R. China.

# These authors contributed equally

*To whom correspondence should be addressed.

E-mail: caofeifei@mail.hzau.edu.cn (Fei-Fei Cao)

Material characterization

TEM images and HAADF-STEM-EDS analysis were performed on FEI Titan Themis 200 transmission electron microscope. XRD patterns are recorded on a Bruker D8 Advance X-ray diffractometer with Cu Kα radiation as the incident X-ray. XPS spectra were obtained on an ESCALAB 250Xi energy spectrometer (Thermo Fisher Scientific). The electrochemical Raman spectroscopy was performed on Renishaw inVia spectrometer with laser wavelength of 532 nm.

Electrochemical measurements

The electrochemical cell used for the three-electrode system was H-type electrolytic cell separated by a piece of Nafion 212 membrane, in which reversible hydrogen electrode (RHE) with "close" compartment [1] was used as the reference electrode and the graphite rod was used as the counter electrode. The electrode with CP as the conductive substrate can be directly used as the working electrode with an effective area of 1 cm×1 cm. For comparison, 20%Pt/C (Alfa Aesar) catalyst was loaded on CP by dispersing Pt/C (1 mg) in 200 μL anhydrous ethanol containing 10 μL Nafion followed by dripping on CP.

All electrochemical tests were performed in standard three-electrode system controlled by a CHI-760E electrochemical workstation. The electrolyte at the working electrode side for HER/OER and HMFOR is 1 M KOH and 1 M KOH + 10 mM HMF, respectively. The LSV curve is performed at a scan rate of 5 mV s^{-1} in N_2-purged electrolyte. Unless otherwise indicated, the measured potentials are *IR*-corrected values, where the ohmic impedance *R* was measured by electrochemical impedance spectroscopy.

The durability of Ni/TiO_2-CP for HER was evaluated at constant and dynamic potential conditions. For constant potential testing, the electrode was controlled at -361 mV (without *IR* correction) for 10 h. The dynamic potential testing was conducted by cycling the potential between -0.392 and 0 V (without *IR* correction) at 100 mV s^{-1} for 5000 cycles.

Assembly and testing of AEM electrolyzer

To test the catalytic performance of Ni/TiO_2-CP for HER, the AEM electrolyzer was assembled by using Ni/TiO_2-CP, nickel foam-supported Ni-Fe hydroxide (Ni-Fe-OH/NF)[2] and FAA-3-50 membrane (Fumatech) as the cathode, anode and AEM, respectively. The AEM was immersed in 1 M KOH for 24 h before use. The anode, cathode, AEM and gaskets were assembled between two gold plated steel plates with serpentine flow field. The effective area of electrode is 4 cm^2. Both cathode and anode are supplied by flowing 1 M KOH which was circulated by pumps. The polarization curve and voltage-time curve at 1000 mA cm^{-2} were recorded by IT-6821 power supply (ITCEH).

To test the catalytic performance of Ni/TiO_2-CP for HMFOR, the AEM electrolyzer was assembled by using nickel foam-supported Pt (Pt/NF),[3] Ni/TiO_2-CP and FAA-3-50 membrane as the cathode, anode and AEM, respectively. The electrolyzer was conducted at anolyte one-pass mode. The HMF solution (20 mM) and KOH solution (2 M) were stored separately, and they were mixed in the pipeline at the same flow rate and then imported into the electrolyzer. The cathode was circulated by 1 M KOH by pump.

Product Quantification

The quantitative analysis of HMF and its oxidation products was performed by HPLC (Aglient 1260) using INERTSUSTAIN C18 column (5 μm, 4.6 mm×250 mm). The reaction solution (100 μL) was diluted to 10 mL to reduce the concentration of HMF and products for HPLC testing. Ultrapure water with 0.1% trifluoroacetic acid and acetonitrile with 0.1% trifluoroacetic acid at a flow rate of 95/5 were used as the mobile phase (1 mL min^{-1}). The wavelength of ultraviolet detector was set at 265 nm. The retention time for HMF, HMFCA, FFCA and FDCA is 10.6 min, 12.8 min, 14.4 min and 18.4 min, respectively. The HMF conversion, FDCA yield, and Faraday efficiency were calculated by equations (1-3).

$$\text{HMF conversion (\%)} = \frac{\text{mol of HMF consumed}}{\text{mol of initial HMF}} \times 100\% \tag{1}$$

$$\text{FDCA yield (\%)} = \frac{\text{mol of FDCA formed}}{\text{mol of initial HMF}} \times 100\% \tag{2}$$

$$\text{Faraday efficiency} = \frac{\text{mol of FDCA formed}\times 6F + \text{mol of HMFCA formed}\times 2F + \text{mol of FFCA formed}\times 4F}{\text{total charge passed}} \times 100\% \tag{3}$$

Theoretical calculation

Ni cluster/TiO_2(110) and Ni(111) model were used to simulate the structure of Ni/TiO_2 interface and Ni site far away from the interface, respectively. The vacuum layer along the z direction is 18 Å, which is sufficient to avoid the interaction between two adjacent regions. H_2O, H*, and HO+H groups, the reactive intermediates of the HER process, are adsorbed on the surface. The two atomic layers at the bottom of the model are fixed, and the three atomic layers at the top are relaxed.

First principles calculations in the density functional theory framework are performed based on the Cambridge Sequential Total Energy Package (CASTEP). The modular conservation pseudopotential under the generalized Gradient approximation (GGA) and the Perdew-Burke-Ernzerhof exchange correlation density functional were used to describe the interelectron interactions. A 750 eV in-plane fluctuation energy cutoff and a 5×7×1 K-point sampling set were used for surface calculations of Ni clusters/TiO_2(110) and Ni(111). The force tolerance of 0.01 eV $Å^{-1}$, the energy tolerance of $5.0x10^{-7}$ eV per atom and the maximum displacement of $5.0×10^{-4}$ Å are considered. Grimme's method for DFT-D correction was taken into account in all calculations.

The calculation formula of adsorption energy is as follows:

$$\Delta E_A = E\left(sub / A\right) - E\left(sub\right) - E_A \qquad (4)$$

where E(sub/A) represents the total energy of A (= H_2O, H* and HO+H groups) on the substrate; E(sub) and E_A are the total energy of bare base and A group, respectively.

The free energy of each reaction step can be calculated by the following formula:

$$\Delta G = \Delta E + \Delta E_{ZPE} - T\Delta S \qquad (5)$$

where ΔE is the adsorption energy calculated by DFT, ΔE_{ZPE} and ΔS are the change of zero point energy and entropy. Set the temperature T to 300 K, $\left(\Delta E_{ZPE} - T\Delta S\right) = 0.26$ eV.

Supplementary Note 1

The conversion temperature of reduction of metal oxide can be used to evaluate the difficulty of metal oxide reduction. On the basis of equation $\Delta_r G_\mathrm{m}^0 = \Delta_r H_\mathrm{m}^0 - T\Delta_r S_\mathrm{m}^0$, the conversion temperature (T_conv) is calculated by the following equation:

$$T_\mathrm{conv} = \frac{\Delta_r H_\mathrm{m}^0}{\Delta_r S_\mathrm{m}^0}$$

The standard thermodynamic properties of related substances are listed below:

	H_2(g)[a]	H_2O(g)[a]	NiO(s)[b]	Ni(s)[a]	TiO_2(s)[a]	Ti(s)[a]
$\Delta_f H_\mathrm{m}^0$ (kJ mol^{-1})	0	-241.8	-240.11	0	-944.0	0
S_m^0 (J mol^{-1} K^{-1})	130.7	188.8	38.0	29.9	50.6	30.7

[a] Data from CRC Handbook of Chemistry and Physics 97th Edition; [b] Data from literature (*Geochimica et Cosmochimica Acta* **1986,** *50* (11), 2439)

For NiO reduction:

$$\mathrm{NiO(s)} + \mathrm{H_2(g)} \rightarrow \mathrm{Ni(s)} + \mathrm{H_2O(g)}$$

$$\begin{aligned}\Delta_r H_\mathrm{m}^0 &= \Delta_f H_\mathrm{m}^0(\mathrm{H_2O,g}) + \Delta_f H_\mathrm{m}^0(\mathrm{Ni,s}) - \Delta_f H_\mathrm{m}^0(\mathrm{NiO,s}) - \Delta_f H_\mathrm{m}^0(\mathrm{H_2,g})\\ &= -241.8 - (-240.11)\\ &= -1.69\ \mathrm{kJ\ mol^{-1}}\end{aligned}$$

$$\begin{aligned}\Delta_r S_\mathrm{m}^0 &= S_\mathrm{m}^0(\mathrm{H_2O,g}) + S_\mathrm{m}^0(\mathrm{Ni,s}) - S_\mathrm{m}^0(\mathrm{NiO,s}) - S_\mathrm{m}^0(\mathrm{H_2,g})\\ &= 188.8 + 29.9 - 38.0 - 130.7\\ &= 50\ \mathrm{J\ mol^{-1}K^{-1}}\end{aligned}$$

$$\Delta_r G_\mathrm{m}^0 < 0$$

For TiO_2 reduction:

$$\mathrm{TiO_2(s)} + 2\mathrm{H_2(g)} \rightarrow \mathrm{Ti(s)} + 2\mathrm{H_2O(g)}$$

$$\begin{aligned}\Delta_r H_\mathrm{m}^0 &= 2\Delta_f H_\mathrm{m}^0(\mathrm{H_2O,g}) + \Delta_f H_\mathrm{m}^0(\mathrm{Ti,s}) - \Delta_f H_\mathrm{m}^0(\mathrm{TiO_2,s}) - 2\Delta_f H_\mathrm{m}^0(\mathrm{H_2,g})\\ &= -2\times 241.8 - (-944)\\ &= 460.4\ \mathrm{kJ\ mol^{-1}}\end{aligned}$$

$$\Delta_r S_{\mathrm{m}}^{0} = 2S_{\mathrm{m}}^{\theta}\left(\mathrm{H_2O,g}\right) + S_{\mathrm{m}}^{0}\left(\mathrm{Ti,s}\right) - S_{\mathrm{m}}^{0}\left(\mathrm{TiO_2,s}\right) - 2S_{\mathrm{m}}^{0}\left(\mathrm{H_2,g}\right)$$
$$= 2\times 188.8 + 30.7 - 50.6 - 2\times 130.7$$
$$= 96.3\ \mathrm{J\ mol^{-1}K^{-1}}$$

$$T_{\mathrm{conv}} = 4781\ \mathrm{K}$$

It can be found that the $\Delta_r G_{\mathrm{m}}^{0}$ of NiO reduction is lower than 0, indicating that the reduction of NiO by H_2 is easy in thermodynamics. In contrast, the T_{conv} of TiO_2 reduction is very high, suggesting that the reduction of TiO_2 is difficult in thermodynamics.

Supplementary Note 2

The average crystal size of Ni (D) is calculated by Scherrer equation: $D = K\lambda / (\beta\cos\theta)$, where K is Scherrer constant (0.89); λ is the incident X-ray wavelength (0.15405 nm); β is the angular line width at half-maximum of the highest intensity in radians, and θ is the corresponding diffraction angle. The values of β and θ are obtained by Gaussian fitting of Ni(111) diffraction peak.

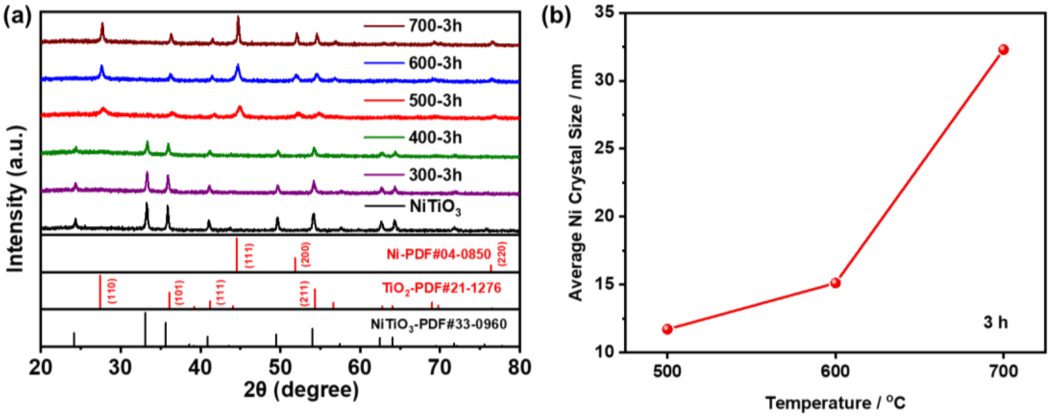

Figure S1. (a) XRD patterns of $NiTiO_3$ and $NiTiO_3$ reduced at different temperatures for 3 h. (b) Average Ni crystal size of Ni/TiO_2 obtained at different temperatures. The crystal size is calculated by Scherrer equation (Supplementary Note 2).

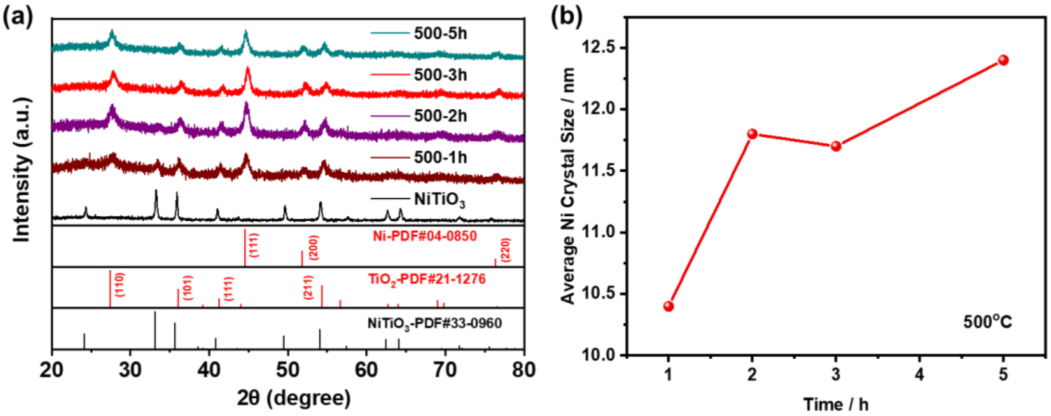

Figure S2. (a) XRD patterns of $NiTiO_3$ and $NiTiO_3$ reduced at 500°C for different time. (b) Average Ni crystal size of product obtained at different time. The crystal size is calculated by Scherrer equation (Supplementary Note 2).

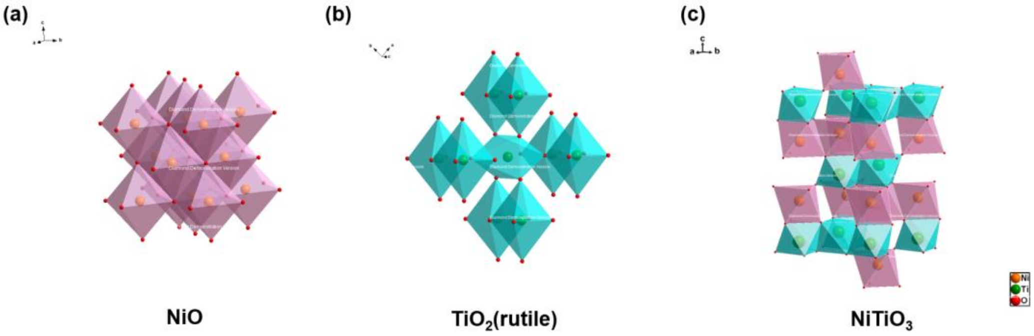

Figure S3. Crystallographic structure of NiO, TiO_2 and $NiTiO_3$.

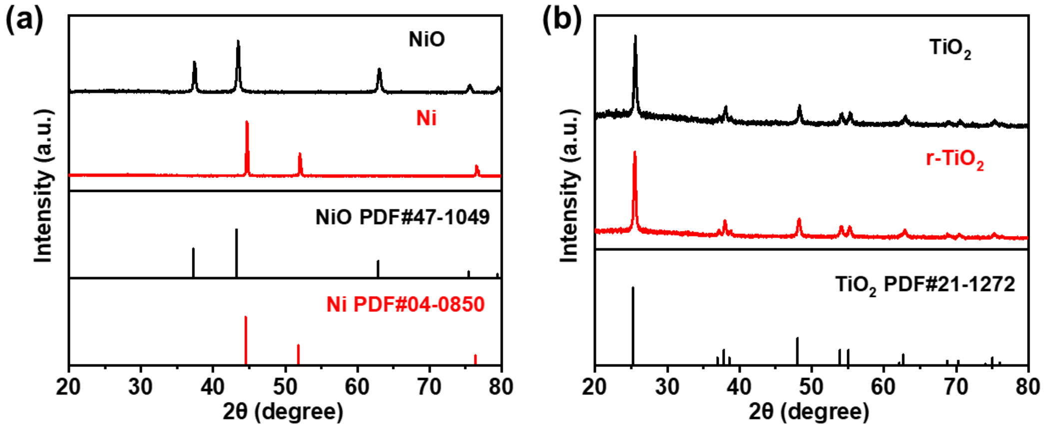

Figure S4. (a) XRD patterns of NiO and Ni. (d) XRD patterns of TiO_2 and r-TiO_2.

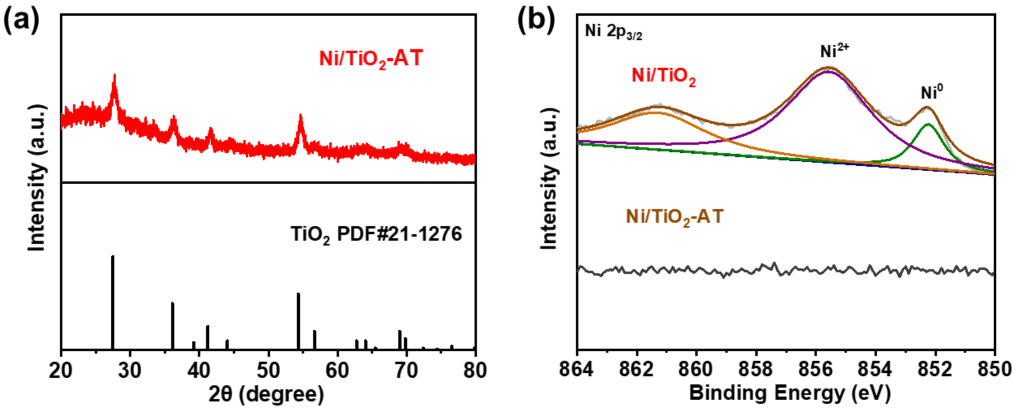

Figure S5. (b) XRD pattern of Ni/TiO_2-AT. (b) Ni $2p_{3/2}$ XPS spectra of Ni/TiO_2 and Ni/TiO_2-AT.

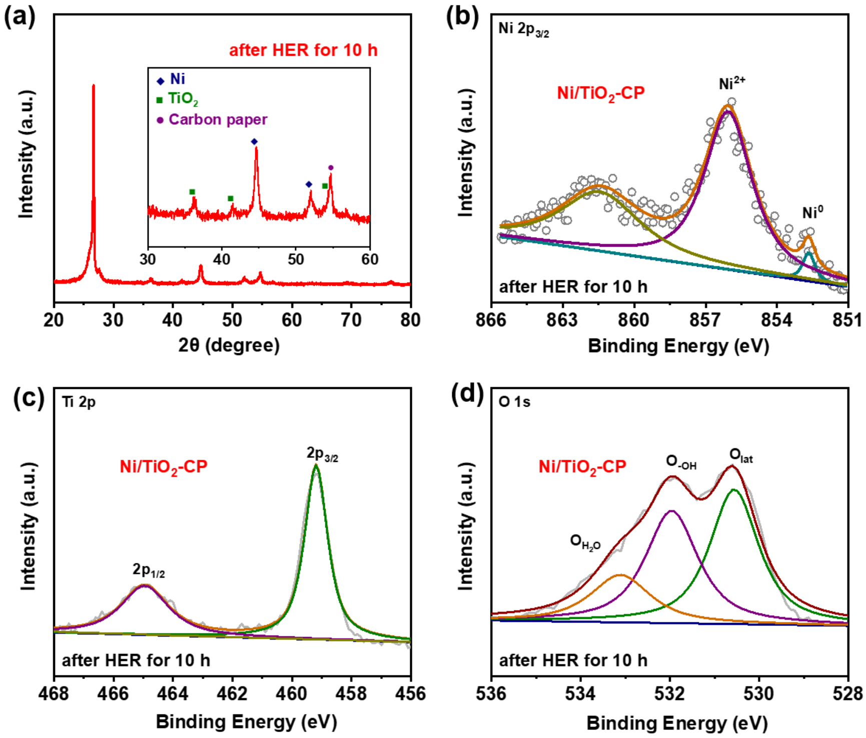

Figure S6. (a) XRD pattern of Ni/TiO_2-CP after catalyzing HER for 10 h in 1 M KOH. (b) Ni $2p_{3/2}$, (c) Ti 2p and (d) O 1s XPS spectra of Ni/TiO_2-CP after catalyzing HER for 10 h in 1 M KOH.

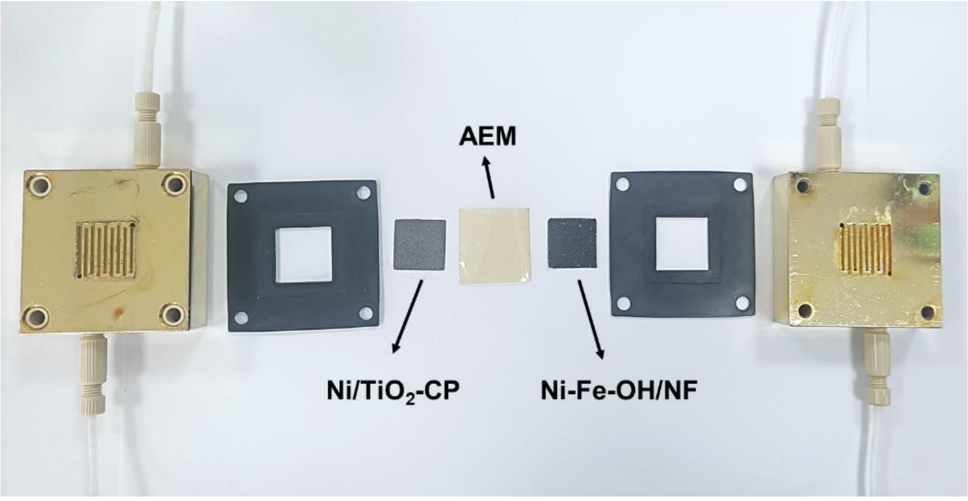

Figure S7. Photograph of AEM electrolyzer with Ni/TiO_2-CP as cathode and Ni-Fe-OH/NF as anode.

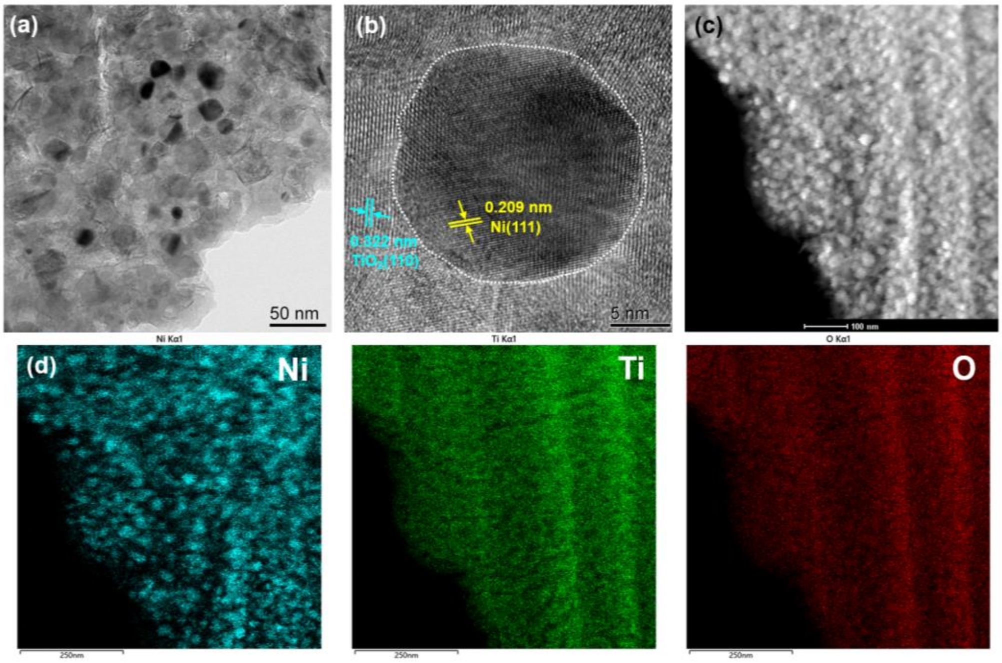

Figure S8. (a) TEM image, (b) HRTEM image, (c) STEM image and (d) elemental mapping of Ni/TiO_2-CP after catalyzing HER in AEM electrolyzer at 1000 mA cm^{-2} for 106 h.

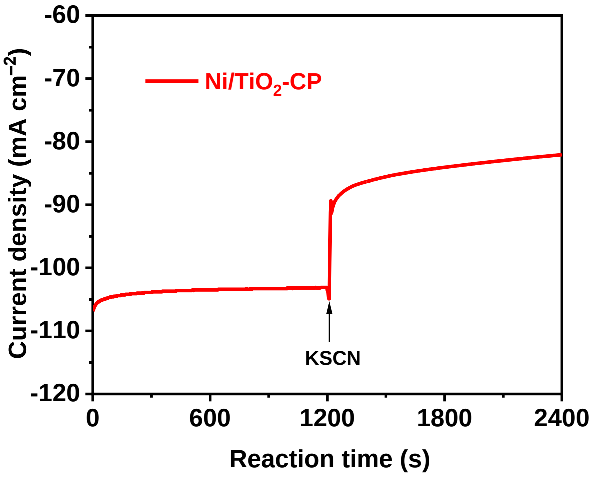

Figure S9. Current change of Ni/TiO_2-CP after the introduction of KSCN during HER in 1 M KOH.

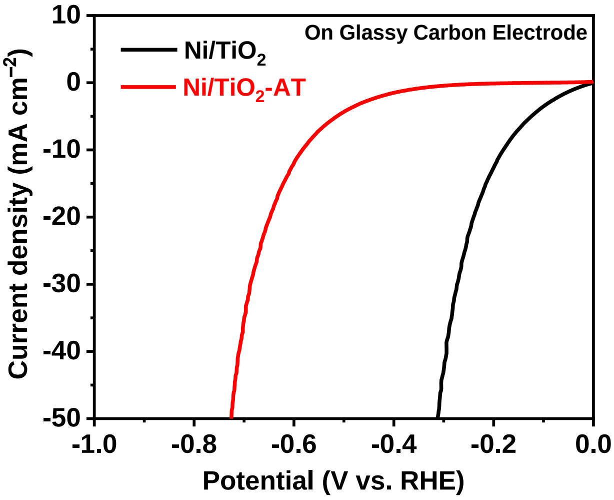

Figure S10. LSV curves of Ni/TiO_2 and Ni/TiO_2-AT on glassy carbon electrode in 1 M KOH.

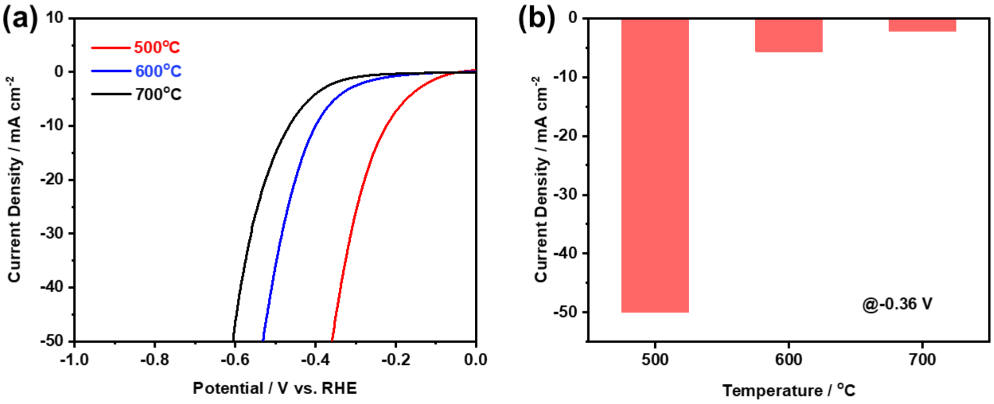

Figure S11. (a) LSV curves of Ni/TiO_2 obtained at different temperature for HER in 1 M KOH. (b) Current density at -0.36 V for different Ni/TiO_2 catalysts. The catalyst is loaded on glassy carbon electrode.

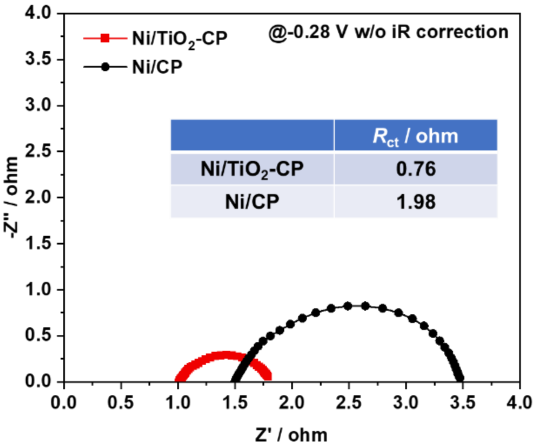

Figure S12. Nyquist curves of Ni/TiO$_2$-CP and Ni-CP during HER. The inset shows the charge transfer resistance for the two electrodes.

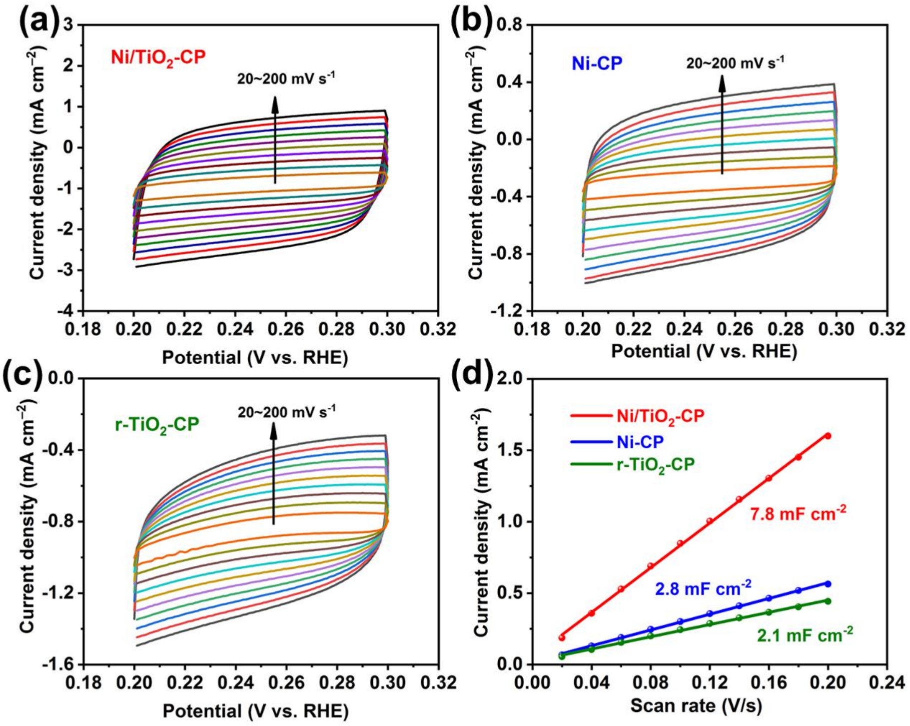

Figure S13. CV curves of (a) Ni/TiO$_2$-CP, (b) Ni-CP and (c) r-TiO$_2$-CP in 1 M KOH. (d) C_{dl} of Ni/TiO$_2$-CP, Ni-CP and r-TiO$_2$-CP.

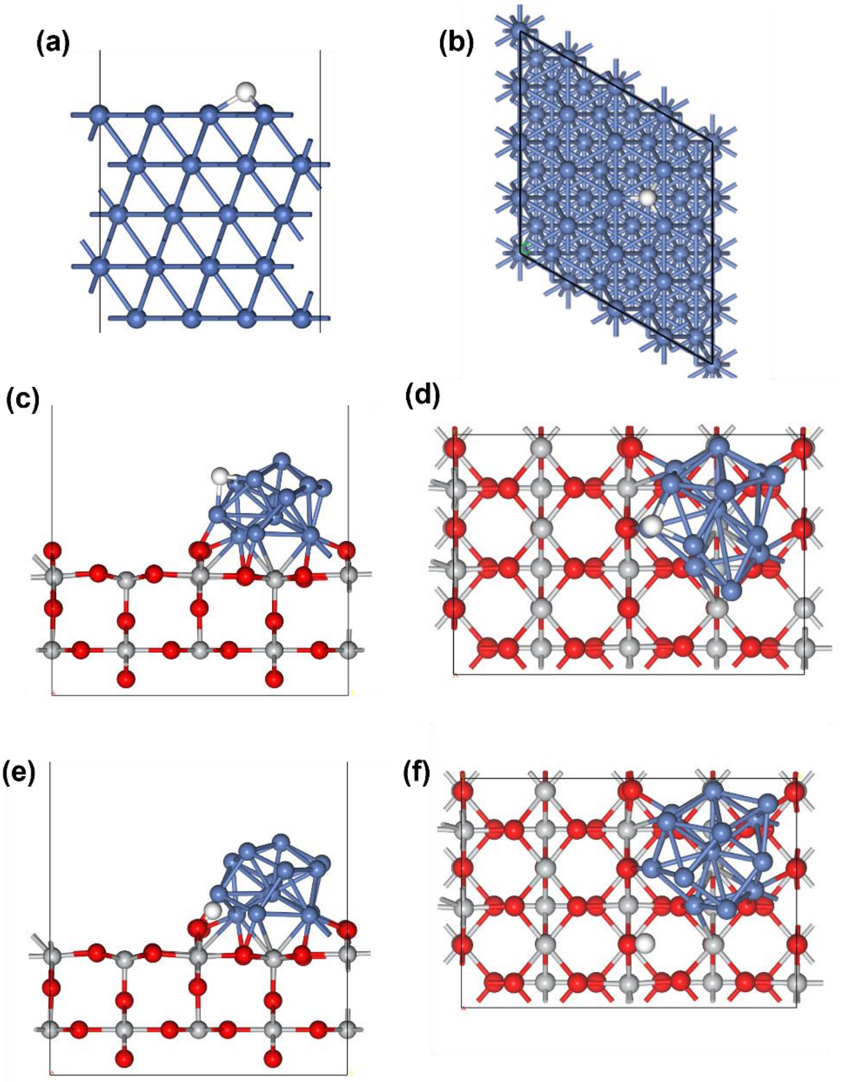

Figure S14. Calculated H_{ad} adsorption configuration on (a-b) Ni(111), (c-d) Ni cluster near the interface and (e-f) TiO_2 near the interface. Ni(111) is used to model the Ni site far away from the Ni/TiO_2 interface, Ni cluster is used to model the Ni site near the Ni/TiO_2 interface.

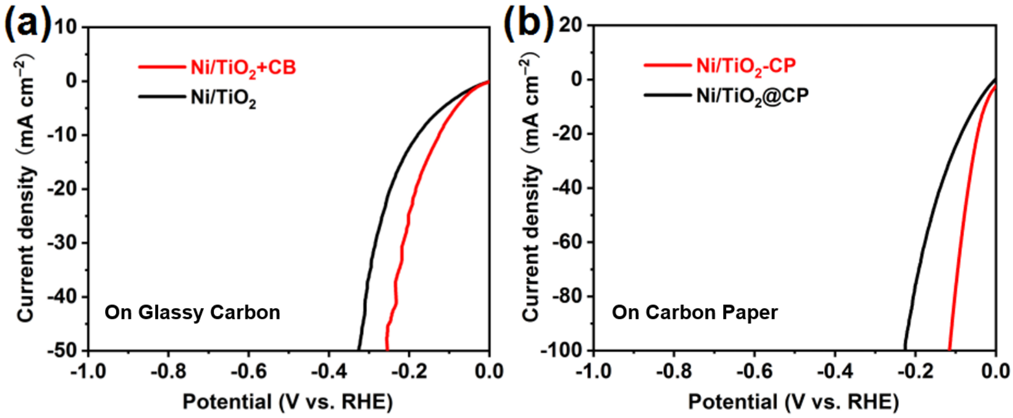

Figure S15. (a) LSV curves of Ni/TiO$_2$ and Ni/TiO$_2$ + carbon black (CB) on glassy carbon electrode in KOH. (b) LSV curves of Ni/TiO$_2$-CP and the Ni/TiO$_2$@CP. Ni/TiO$_2$+CB working electrode is prepared by adding CB into the Ni/TiO$_2$ slurry followed by dropping onto the glassy carbon electrode. Ni/TiO$_2$@CP is prepared by dropping Ni/TiO$_2$ slurry onto CP at the same catalyst loading with Ni/TiO$_2$-CP.

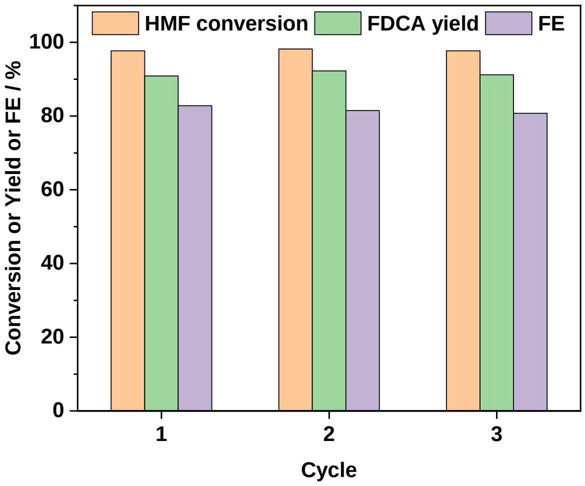

Figure S16. Conversion of HMF, yield of FDCA and Faraday efficiency of Ni/TiO$_2$-CP during HMF oxidation for successive three times at 1.45 V. The data at the theoretical charge is presented.

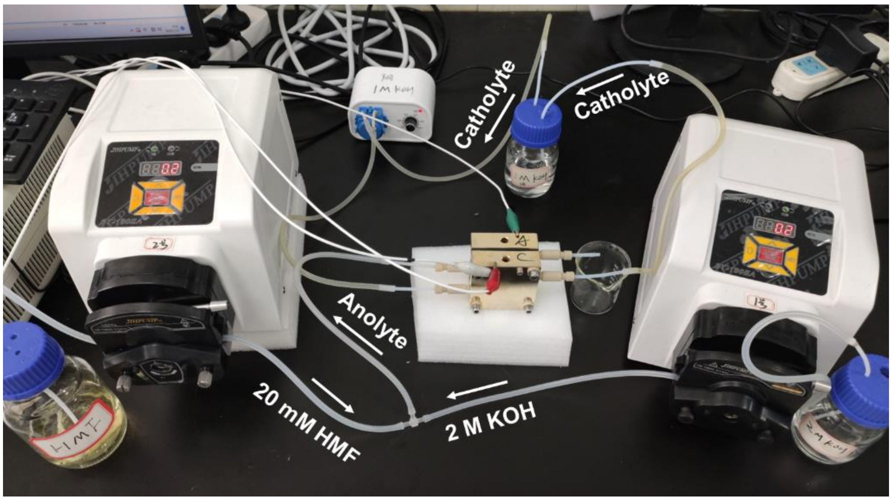

Figure S17. Production of FDCA by AEM electrolyzer on anolyte one-pass mode.

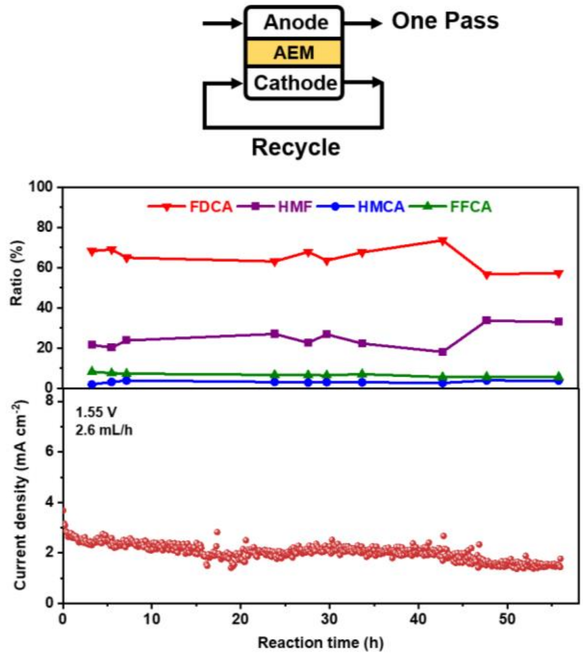

Figure S18. Current and product composition of a single AEM electrolyzer at 1.55 V on anolyte one-pass mode with a rate of 2.6 mL h^{-1} for both flow rates of HMF and KOH solution.

At the HMF solution (20 mM) flow rate of 2.6 mL h^{-1} and cell voltage of 1.55 V, the FDCA content in the product obtained at the outlet of AEM electrolyzer is in the range between 60% and 75%, and that of HMF is between 15% and 35%, indicating that HMF has not been fully converted.

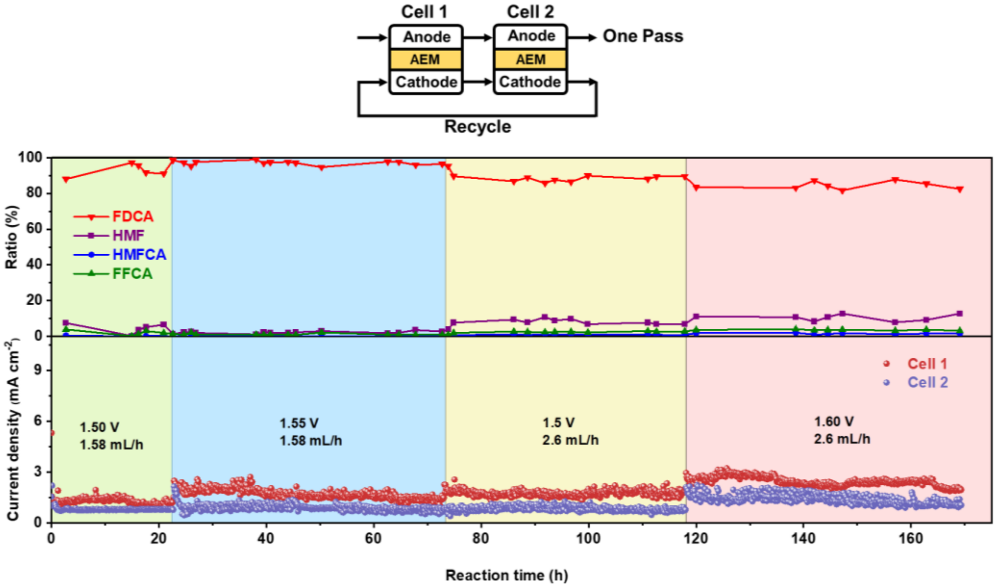

Figure S19. Current and product composition of AEM electrolyzer on anolyte one-pass mode, where the same two electrolyzers are connected in series, the cell voltage is set at 1.50, 1.55 or 1.60 V and both flow rates of HMF and KOH solution are 1.58 or 2.6 mL h^{-1} at the anode.

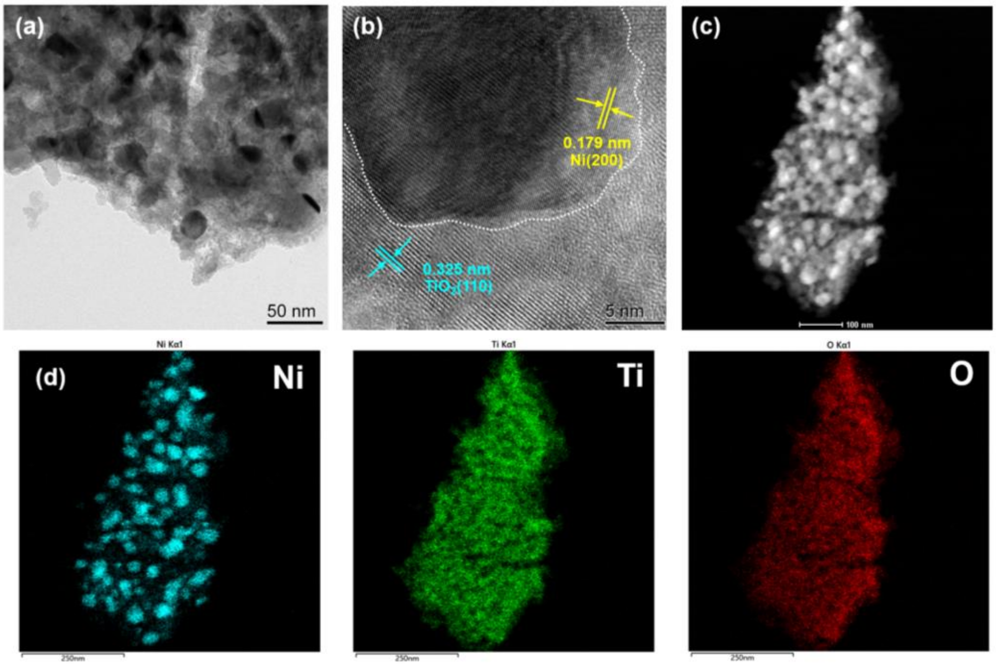

Figure S20. (a) TEM image, (b) HRTEM image, (c) STEM image and (d) elemental mapping of Ni/TiO$_2$-CP after catalyzing HMF oxidation in AEM electrolyzer for 169 h.

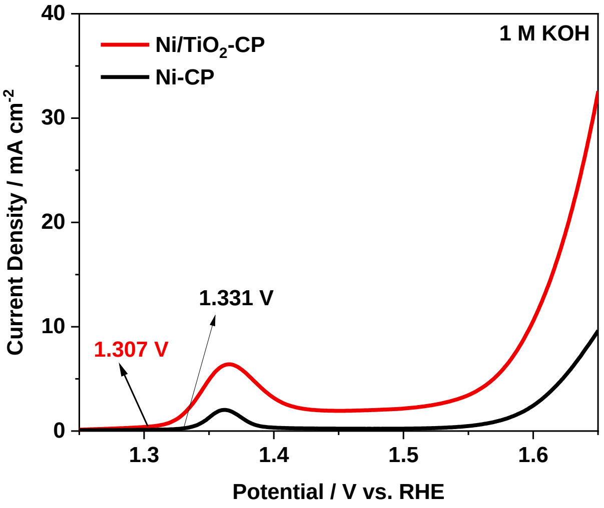

Figure S21. LSV curves of Ni/TiO$_2$-CP and Ni-CP in 1 M KOH.

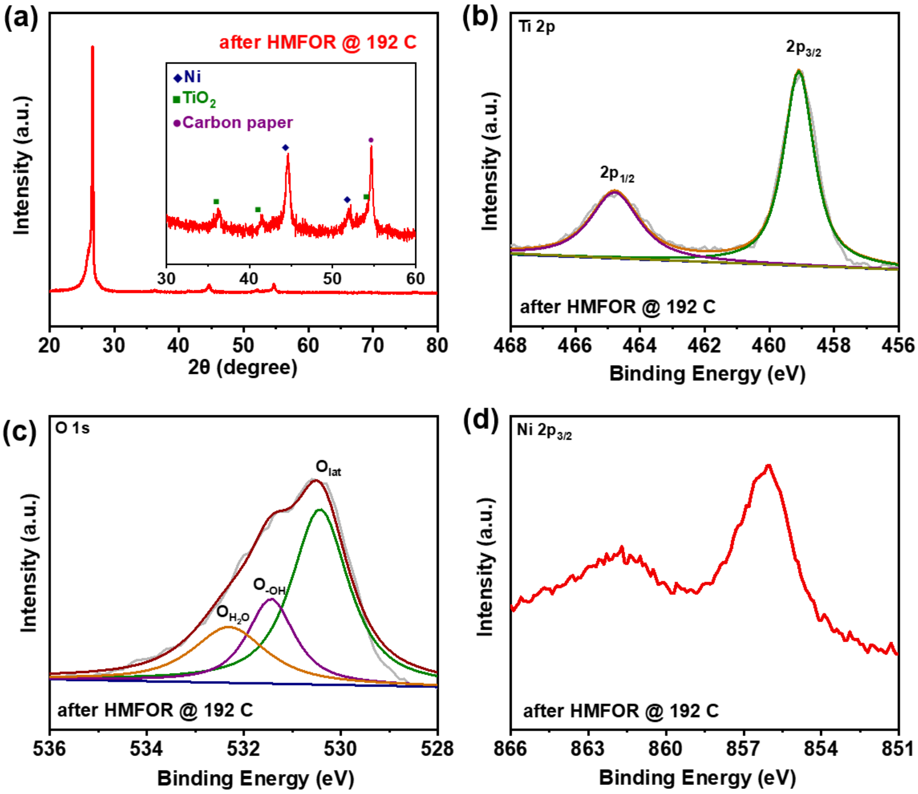

Figure S22. (a) XRD pattern, (b) Ti 2p, (c) O 1s and (d) Ni 2p$_{3/2}$ XPS spectra of Ni/TiO$_2$-CP after HMF oxidation.

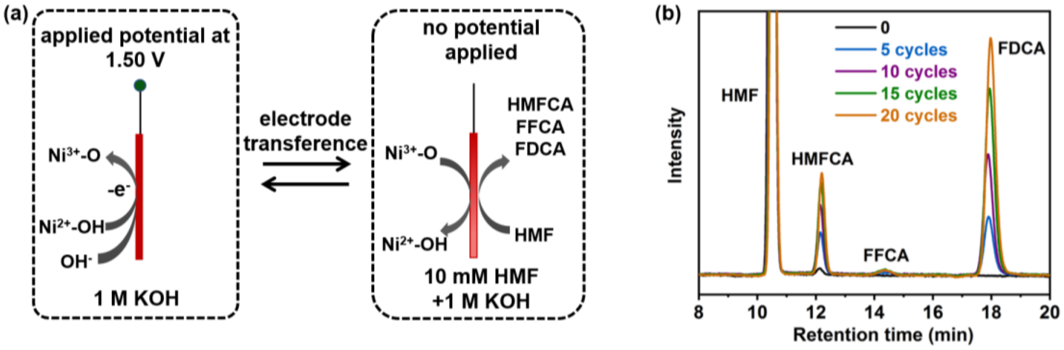

Figure S23. (a) Illustration of the formation of Ni^{3+}-O species on Ni/TiO_2-CP and the spontaneous reaction between Ni^{3+}-O species and HMF. (b) HPLC chromatogram traces of solution after different reaction cycles shown in panel (a).

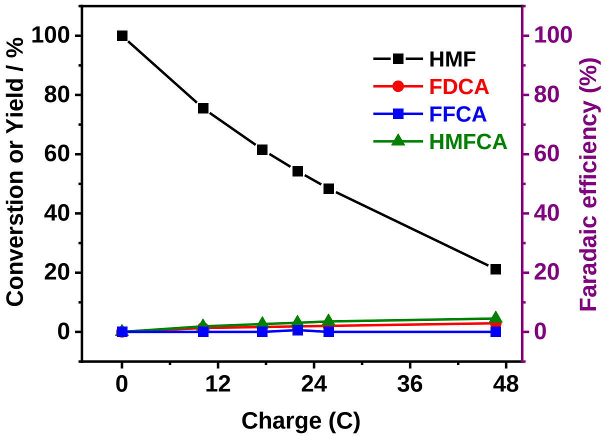

Figure S24. Conversion of HMF and yield of various products during oxidation at 1.30 V using Ni/TiO_2-CP as the electrode in 1 M KOH + 10 mM HMF.

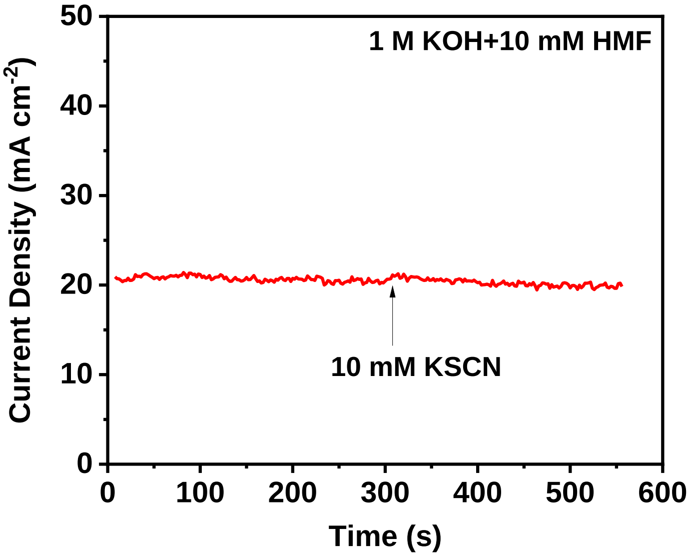

Figure S25. Current change of Ni/TiO_2-CP after the introduction of KSCN during HMF oxidation in 1 M KOH+10 mM HMF.

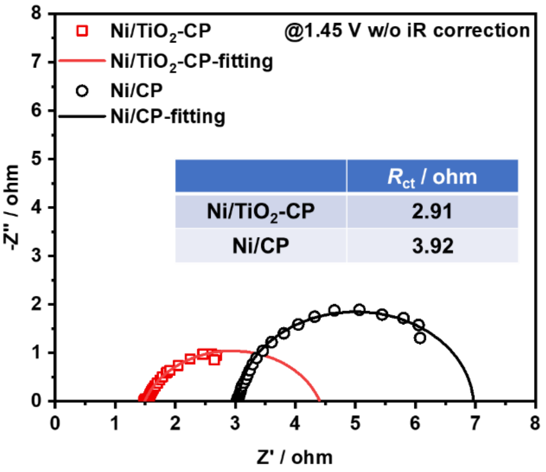

	R_{ct} / ohm
Ni/TiO_2-CP	2.91
Ni/CP	3.92

Figure S26. Nyquist curves of Ni/TiO_2-CP and Ni-CP during HMF oxidation. The inset shows the charge transfer resistance for the two electrodes.

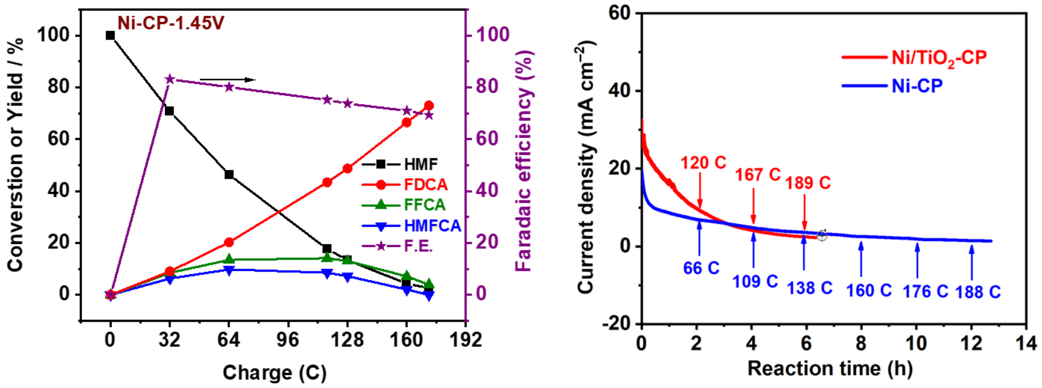

Figure S27. (a) Conversion of HMF, yield of various products and Faraday efficiency during oxidation at 1.45 V using Ni-CP as the electrode in 1 M KOH + 10 mM HMF. (b) The change of current with time during HMF oxidation for Ni/TiO$_2$-CP and Ni-CP.

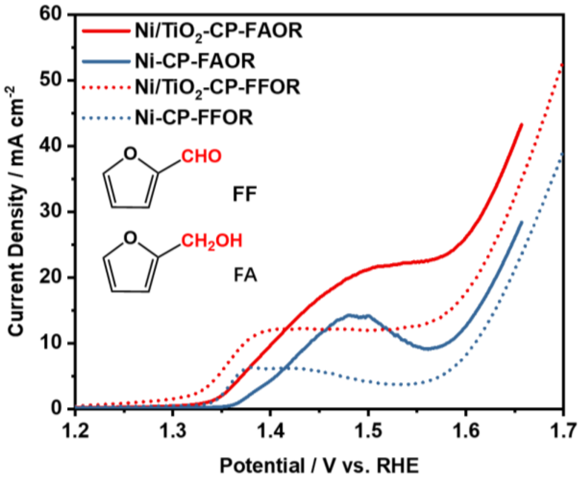

Figure S28. LSV curves of Ni/TiO$_2$-CP and Ni-CP in 1 M KOH with 10 mM furfural (FF) or 10 mM furfuryl alcohol (FA).

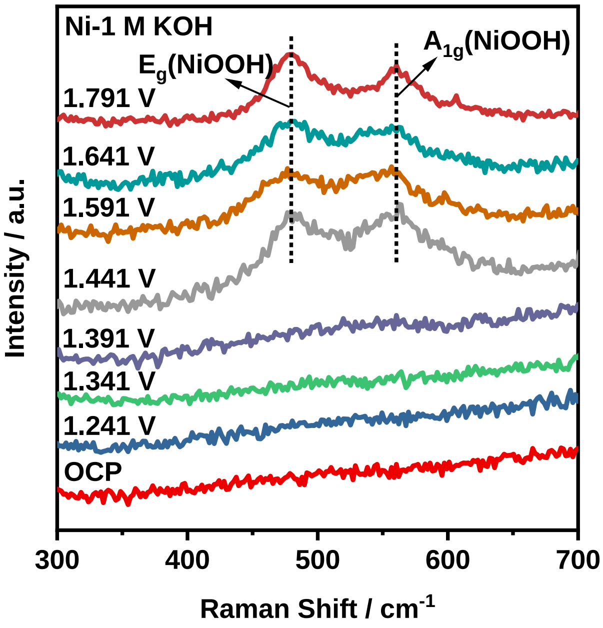

Figure S29. In-situ Raman spectra of Ni in 1 M KOH.

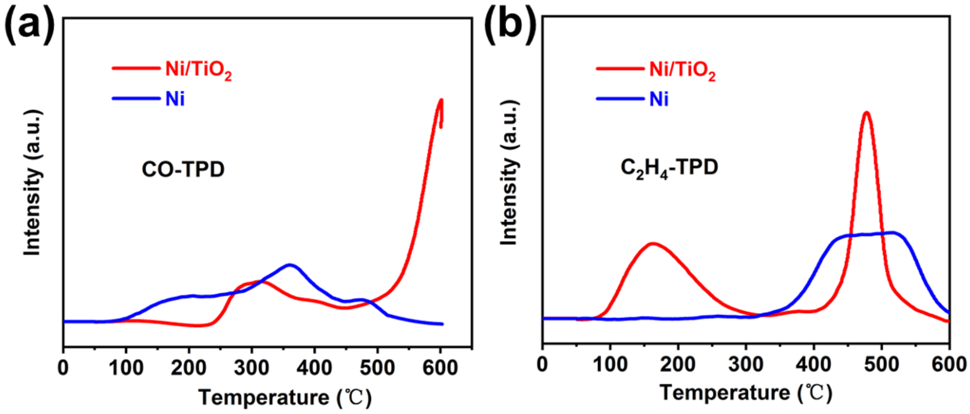

Figure S30. (a) CO-TPD curves of Ni/TiO_2 and Ni. (b) C_2H_4-TPD curves of Ni/TiO_2 and Ni.

Temperature programmed desorption (TPD) technique is employed to evaluate the adsorption of HMF on catalyst. There are C=O and C=C in the molecule of HMF, so CO and C_2H_4 are used as the adsorbent in TPD.[4] The desorption of CO on Ni starts from ~100°C, while that on Ni/TiO_2 starts at ~240°C, indicating the stronger adsorption of CO on Ni/TiO_2. The desorption of C_2H_4 on Ni starts from ~330°C. In comparison, there are two C_2H_4 desorption peaks on Ni/TiO_2. The first desorption peak starts at a temperature lower than 100°C, which is probably resulted from the desorption of physical adsorbed C_2H_4. The second C_2H_4 desorption peaks starts at ~420°C, which should be ascribed to the chemical adsorbed C_2H_4. The above results imply that the adsorption of HMF on Ni/TiO_2 is enhanced with respect to Ni.

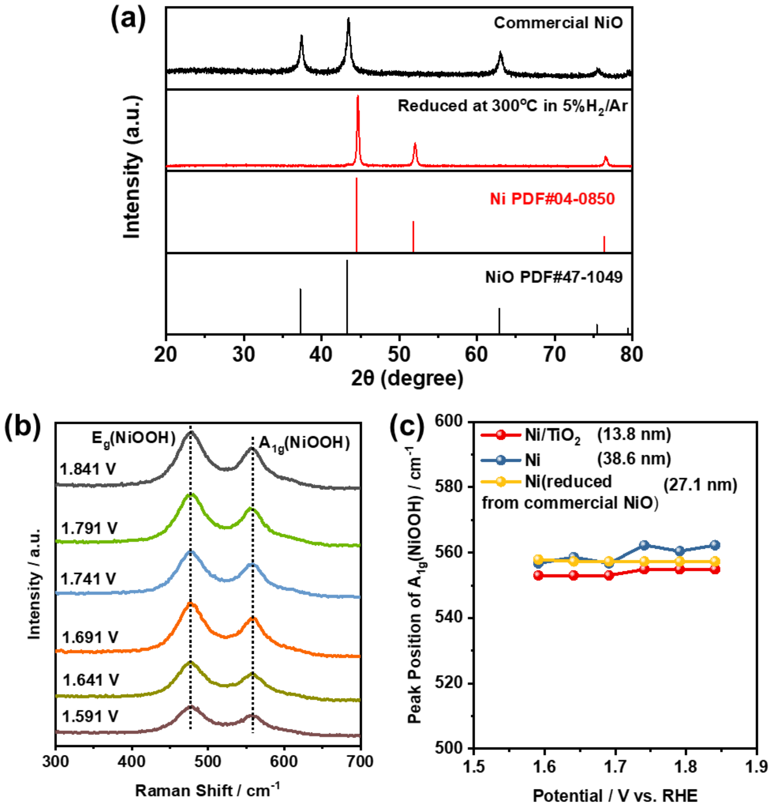

Figure S31. (a) XRD patterns of commercial NiO and its reducing product. (a) In-situ Raman spectra of Ni nanoparticles reduced from commercial NiO in 1 M KOH. (b) The wavenumber of A_{1g} mode of NiOOH for Ni/TiO_2, Ni and Ni nanoparticles reduced from commercial NiO at different potentials.

The Ni nanoparticles with an average particle size of 27.1 nm are obtained by reducing commercial NiO nanoparticles (12.5 nm in average particle size) at 300°C for 2 h in 5%H_2/Ar. The particle size of Ni nanoparticles is calculated by Scherrer equation (Supplementary Note 2). It is found that the wavenumber of A_{1g} mode of NiOOH is negatively shifted with the decrease of Ni particle size.

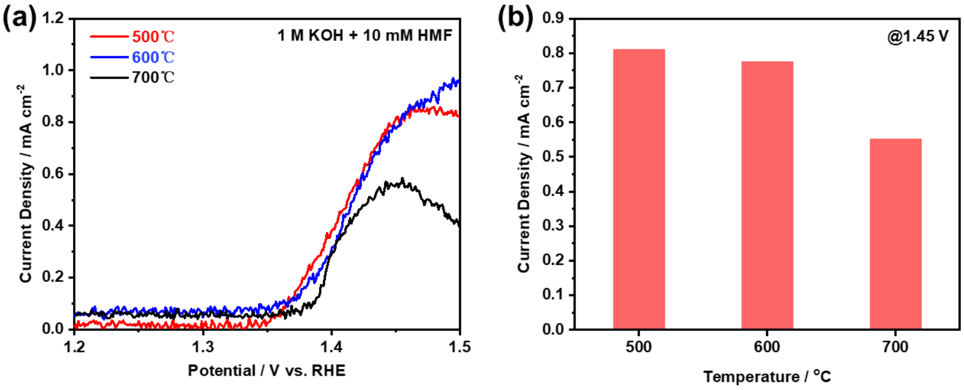

Figure S32. (a) LSV curves of Ni/TiO_2 obtained at different temperature for HMF oxidation in 1 M KOH+10 mM HMF. (b) Current density at 1.45 V for different Ni/TiO_2 catalysts. The catalyst is loaded on glassy carbon electrode.

Table S1 The HER performance of Ni/TiO_2-CP and other TiO_2-based catalysts in 1 M KOH.

Catalyst	**η at 10 mA cm^{-2} (mV)**	**$\Delta\eta/\Delta\log(\lvert j\rvert)^a$ (mV dec^{-1})**	**Durability (h)**	**Reference**
Ni/TiO_2-CP	28	71	106 h@1000 mA cm^{-2}	This Work
Ti/TNTs/CoOP	130	97	24 h@10 mA cm^{-2}	Electrochim. Acta 2023, 456, 142436
Ru/TNTA	38	46	n.a.	J. Power Sources 2023, 562, 232747
FeS_x/TNT	343	n.a.	n.a.	ChemSusChem 2023, 16 (11), e202300115
Ru/P-TiO_2	27	76	24 h@~10 mA cm^{-2}	Angew. Chem., Int. Ed. 2022, 61 (47), e202212196
TiO_2-CoP/NF	61	64	24 h@10 mA cm^{-2}	J. Energy Chem. 2022, 74, 111
RuO_2@TiO_2/TP	30	100	24 h@100 mA cm^{-2}	Inorg. Chem. Front. 2022, 9 (24), 6602
NF/(Ni_3S_2-MoS_2)@TiO_2	49	67	200 h@20 mA cm^{-2}	Small 2022, 18 (24), 2201896
TiO_2@Co_3O_4(E)	26	80	50 h@20 mA cm^{-2}	J. Mater. Chem. A 2022, 10 (26), 13769
D-RuO_2/TiO_2/TM	10	87	18 h@n.a.	Chem. Eng. J. 2022, 431, 134072
Ru@TiO_2-V	34	87	200 h@~300 mA cm^{-2}	Chem. Eng. J. 2022, 446, 137248
CoP_3/CoMoP/TiO_{2-x}@Ti	143	64	48 h@~15 mA cm^{-2}	J. Alloy. Compd. 2022, 905, 164165.
NC/Ni/TiO_2	65	193	15 h@48 mA cm^{-2}	Appl. Catal., B 2021, 282, 119548
Co-TiO_2@Ti(H_2)	78	117	10 h@480 mA cm^{-2}	Small Methods 2021, 5, 2100246
Ni/TiO_2-form-A-II	46	50	24 h@~10 mA cm^{-2}	J. Mater. Chem. A 2021, 9 (10), 6325
Ru/r-TiO_2	15	50	10 h@~10 mA cm^{-2}	Nano Energy 2021, 88, 106211
TiO_2@WS_2	142	83	24 h@-0.3 V	Int. J. Hydrogen Energy 2020, 45 (3), 1697

[a] $\Delta\eta/\Delta\log(\lvert j\rvert) = (\eta@50\ mA\ cm^{-2} - \eta@10\ mA\ cm^{-2})/(\log50 - \log10)$

Table S2 The HER performance of Ni/TiO_2-CP and other catalysts in 1 M KOH. The noble metal-based catalysts are marked by blue color and noble metal-free catalysts are marked by green color.

Catalyst	**η at 10 mA cm^{-2} (mV)**	**$\Delta\eta/\Delta\log(\lvert j\rvert)^a$ (mV dec^{-1})**	**Durability (h)**	**Reference**
Ni/TiO_2-CP	28	71	106 h@1000 mA cm^{-2}	This Work
Pt_3Fe/NMCS-A	29	116	10 h@10 mA cm^{-2}	Adv. Mater. 2023, 2303030.
Pt_{SA}-Pt_C/NDPCM	20	81	60 h@10 mA cm^{-2}	Adv. Funct. Mater. 2023, 2304852.
cRu-Ni_3N/NF	32	54	100 h@50 mA cm^{-2}	Energy Environ. Mater., 2023, 6, e12318
Ru@Ni-MOFs/NF	25	49	80 h@10 mA cm^{-2}	Chem. Eng. J. 2023, 451, 138618
Ru SAs-SnO_2/C	10	71	27 h@~10 mA cm^{-2}	Angew. Chem., Int. Ed. 2022, 61, 202209486
RhP_2@NPG	34.7	58	40 h@50 mA cm^{-2}	Adv. Mater. 2022, 35, 2207114.
Ru-$NiCo_2O_4$ NSs	117	119	42 h@10 mA cm^{-2}	Chin. Chem. Lett., 2022, 33, 4930
$PdSe_2$ nanosheets	138	146	10 h@25 mA cm^{-2}	Adv. Funct. Mater., 2021, 31, 2102321.
Fe_2P-CoP/CeO_2-20	45	79	30 h@25 mA cm^{-2}	Chem. Eng. J. 2023, 451, 138550
MoO_x/MoNi/CP	35	61	8 h@100 mA cm^{-2}	Chem. Eng. J. 2023, 469, 143846
F-NiO/Ni@C	46	71	50 h@10 mA cm^{-2}	Adv. Funct. Mater. 2023, 2303986.
Ni_2P–$NiMoO_x$/NF	91	70	200 h@100 mA cm^{-2}	ACS Catal. 2023, 13 (14), 9792
NiMo/$CoMoO_4$/NF	102	364	30 h@20 mA cm^{-2}	ACS Appl. Energy Mater. 2023, 10.1021/acsaem.3c01146
P-Ni MOF/POM	35	67	120 h@~120 mA cm^{-2}	J. Mater. Chem. A 2023, 10.1039/D3TA02610H
MoS_2/$NiPS_3$	112	93	100 h@10 mA cm^{-2}	Adv. Mater. 2022, 34 (37), 2203615.
Ni-WO_2/NF	41	84	100 h@100 mA cm^{-2}	Adv. Energy Mater., 2022, 12, 2103301.
N-WS_2/Co_3N	67	90	40 h@100 mA cm^{-2}	Small, 2022, e2203171
CuS@$MoSe_2$	72	80	20 h@11 mA cm^{-2}	ACS Nano 2022, 16, 15425
OH-Ni/Ni_3C	72	119	20 h@100 mA cm^{-2}	Angew. Chem., Int. Ed., 2022, 61, e202206077

Ni/Yb_2O_3	20	57	360 h@500 mA cm^{-2}	Nat. Commun., 2022, 13, 3857
Ni-SN@C	28	96	40 h@11 mA cm^{-2}	Adv. Mater. 2021, 33, 2007508.
Mo-NiP_x/NiS_y	85	83	25 h@200 mA cm^{-2}	Adv. Funct. Mater., 2021, 31, 2101532
NiP_2/$NiSe_2$	89	87	91 h@10 mA cm^{-2}	Appl. Catal., B, 2021, 282, 119584
SAP-Mo_2C-CS	36	63	11 h@20 mA cm^{-2}	Angew. Chem., Int. Ed., 2020, 59, 23791
$Nb_4N_{5-X}O_X$-MoS_2	67	111	30 h@10 mA cm^{-2}	ACS Nano 2020, 14, 4925
$NiS_{0.5}Se_{0.5}$/NF	70	136	300 h@100 mA cm^{-2}	Adv Mater 2020, 32, e2000231

[a] $\Delta\eta/\Delta\log(|j|) = (\eta@50\ \text{mA cm}^{-2} - \eta@10\ \text{mA cm}^{-2})/(\log50 - \log10)$

Table S3 The HMF electrooxidation performance of Ni/TiO_2-CP and other catalysts. The electrolysis is performed in 1 M KOH + 10 mM HMF unless otherwise specified.

Catalyst	**Onset potential (V_{RHE})**	**FDCA yield(%)@Reaction potential(V_{RHE})**	**Durability**	**Reference**
Ni/TiO_2-CP	1.335	91@1.45	>160 h	This Work
NiFe-1	1.362	96@1.478	6 cycles	Angew. Chem., Int. Ed. 2023, 62, e202215804.
$Mn_{0.2}$NiS/GF	1.311	97.3@(1.49 to 1.78 V)	10 cycles	Adv. Funct. Mater. 2023, 33, 2214488
14%Ce-$Ni(OH)_2$	1.355	95.5@1.486	6 cycles	Inorg. Chem. 2023, 62 (16), 6499
CuO-PdO	1.14	96.2@n.a.	6 cycles	Adv. Mater. 2022, 34, 2204089
Pt_1Ni_3 NWs	1.315	98@n.a.	6 cycles	ACS Nano 2022, 16, 21518
Ni_3S_2-MoS_2/NF	1.32	100@1.4	5 cycles 8 h	Small 2022, 18, 2201306.
Ru_1-NiO	1.2	90@1.5	n.a.	Angew. Chem., Int. Ed. 2022, 61, 202200211
$Ni_3(PO_4)_2$	1.31	94.2@1.464	5 cycles	ACS Sustainable Chem. Eng. 2022, 10, 5538
Co_3O_4/CF	1.25	96.4@1.4	6 cycles	Appl. Catal., B 2022, 307, 121209
Pt/$Ni(OH)_2$	1.35	98.7@n.a.	n.a.	Angew. Chem., Int. Ed. 2021, 60, 22908
CoFe@NiFe LDH	1.25	100@1.4	n.a.	Adv. Funct. Mater. 2021, 31, 2102886
Ir-Co_3O_4	1.15	98@1.42	6 cycles	Adv. Mater. 2021, 33, 2007056
Vo-Co_3O_4	1.35	91.9@1.47	6 cycles	Adv. Mater. 2021, 34, 2107185
Ni(NS)/CP	1.33	99@1.36	3 cycles	Angew. Chem., Int. Ed. 2021, 60, 14528
t-Ni_1Co_1-MOF	1.28	100@n.a.	5 cycles	Appl. Catal., B 2020, 278, 119339.
MoO_2-FeP@C	1.35	98.6@1.424	10 cycles	Adv. Mater. 2020, 32, 2000455
Ni_3N@C	1.35	98@1.45	6 cycles	Angew. Chem., Int. Ed. 2019, 58, 15895

References of Supporting Information

(1) Jerkiewicz, G. Standard and Reversible Hydrogen Electrodes: Theory, Design, Operation, and Applications. *ACS Catal.* **2020**, *10*, 8409-8417, DOI https://doi.org/10.1021/acscatal.0c02046.

(2) Li, Y.-K.; Zhang, G.; Huang, H.; Lu, W.-T.; Cao, F.-F.; Shao, Z.-G. Ni17W3–W Interconnected Hybrid Prepared by Atmosphere- and Thermal-Induced Phase Separation for Efficient Electrocatalysis of Alkaline Hydrogen Evolution. *Small* **2020**, *16*, 2005184, DOI https://doi.org/10.1002/smll.202005184.

(3) Zhao, H.-F.; Yue, Y.-T.; Fan, Y.-L.; Wang, J.-X.; Li, W.-H.; Wei, F.; Liu, M.; Yu, Y.-H.; Lu, W.-T.; Zhang, G. In-situ Electrochemical Transformed Cu Oxide from Cu Sulfide for Efficient Upgrading of Biomass Derived 5-Hydroxymethylfurfural in Anion Exchange Membrane Electrolyzer. *ChemSusChem* **2022**, *15*, 202201625, DOI https://doi.org/10.1002/cssc.202201625.

(4) Lu, Y.; Liu, T.; Dong, C.-L.; Huang, Y.-C.; Li, Y.; Chen, J.; Zou, Y.; Wang, S. Tuning the Selective Adsorption Site of Biomass on Co3O4 by Ir Single Atoms for Electrosynthesis. *Adv. Mater.* **2021**, *33*, 2007056, DOI https://doi.org/10.1002/adma.202007056.